RSC Advances

PAPER

View Article Online
View Journal | View Issue

Cite this: *RSC Adv.*, 2025, **15**, 30466

Rhodamine and functionalised azobenzene condensed fluorescent *turn on* novel receptor for the selective and sensitive detection of Hg^{2+}: a combined experimental and theoretical study

Pradeep Sahu,†[a] Amit Kumar Chaturwedi,†[a] Ashok Raj Patel,†[b] Abhilash Pandey,†[b] Vanshika Sharma,†[b] Balaji Wamanrao Matore,†[c] Jagadish Singh,[c] Partha Pratim Roy,[c] Milan Hait*[a] and Goutam Kumar Patra*[b]

Received 1st June 2025
Accepted 14th August 2025

DOI: 10.1039/d5ra03890a

rsc.li/rsc-advances

Rhodamine dye has a high absorption coefficient, fluorescence quantum yield, photostability, and extended wavelengths that make it a promising fluorescent probe. A rhodamine and functionalised azobenzene condensed novel chemosensor L has been reported for the first time to detect Hg^{2+} in aqueous ethanol optically in this investigation. Chemosensor L's fluorescence activation in response to Hg^{2+} is due to the suppression of PET and CHEF processes and the change from spirolactam to ring-opened amide. Time-resolved photoluminescence studies confirmed the PET and CHEF processes, whereas ^{13}C-NMR and infrared spectroscopy confirmed the spirolactam ring opening. The opened spirolactam ring forms a 1 : 1 binding complex with Hg^{2+}, as shown by its high binding constant. L can be successfully applied for the formation of a INHIBIT type of logic gate and real sample analysis.

1 Introduction

Environmental pollution has received considerable attention due to its detrimental impacts on ecosystems and human health. Pollution entails the emission of deleterious compounds into the atmosphere, soil, and water due to diverse natural, household, and industrial activities. Principal sources of pollution include industrial processes, transportation, agricultural activities, and natural leaching, which release detrimental pollutants such as carbon dioxide, methane, nitrogen oxides, heavy metals, toxic chemicals, and fine particulates into the environment, thereby substantially exacerbating global climate change.[1] Water contamination chiefly arises from the release of toxic chemicals, heavy metals, and untreated sewage, negatively impacting aquatic ecosystems and human health.[2] Soil contamination sometimes arises from the indiscriminate use of pesticides in agriculture and the improper disposal of industrial waste, resulting in diminished soil fertility.[3] These sources of pollution pose a substantial danger to world biodiversity and environmental sustainability.[4–6]

Metal contamination, encompassing lead, cadmium, mercury, and arsenic, predominantly arises from natural weathering, industrial processing, and agricultural practices, presenting a substantial risk to ecological systems. These metals accumulate in organisms and promote biomagnification along food chains from lower to higher trophic levels.[7,8] Ecosystems contaminated by metals demonstrate inhibited plant growth, diminished microbial diversity, and impaired aquatic systems, leading to deleterious consequences on related creatures.[9] An initiative has commenced to mitigate metal pollution in the ecosystem by microbial bio-accumulation of metal ions and phyto-remediation, with the objective of environmental preservation.[10–14]

Hg^{2+} is associated to a number of health problems, including the well-known Minamata disease, and is recognised as a detrimental contaminant in ecosystems. Because it cannot break down in biological systems or food chains, it poses a serious risk to both human health and the stability of the ecosystem.[15,16] Exposure to Hg^{2+} can also harm the kidneys, brain, endocrine system, and neurological system.[17] Cement kilns, power plants, mercury vapour lamps, barometers, chlor-alkali facilities, gold extraction procedures, and thermometers are some of the notable sources of mercury exposure.[18,19] Mercury's strong attraction to thiol groups in proteins and enzymes disrupts human biological processes. According to the US EPA, the maximum amount of Hg^{2+} in water is two parts per billion.[20]

[a]*Department of Chemistry, Dr C.V. Raman University, Kota, Bilaspur, Chhattisgarh-495113, India. E-mail: haitmilan@gmail.com; pradeepsahu558@gmail.com; amitchaturwedi1@gmail.com*

[b]*Department of Chemistry, Guru Ghasidas Vishwavidyalaya, Bilaspur, Chhattisgarh-495009, India. E-mail: patra29in@yahoo.co.in; ashokquanto@gmail.com; abhilash.pande1992@gmail.com; sharma.vanshika1004@gmail.com*

[c]*Laboratory of Drug Discovery and Ecotoxicology, Department of Pharmacy, Guru Ghasidas Vishwavidyalaya (A Central University), Bilaspur, Chhattisgarh-495009, India*

† These authors contributed equally to this work.

High amounts of Hg^{2+} are commonly found in products such as eye protection, antibacterial soaps, cosmetics, and skin-whitening treatments. This metal can build up in the body by consumption, inhalation, or skin absorption. Methyl mercury exposure can occur from eating fish and from coming into contact with cosmetics. Mercury exposure during pregnancy has been associated with neuro-developmental deficits in the fetus.[21,22] Mercury exposure is usually associated by psychological difficulties, changes to rashes, poorer resistance to skin diseases, and skin pigmentation.[23] Some products do not declare the presence of mercury, which could put the users and their immediate family members in danger. While drinking water can only contain up to 2 parts per million of Hg^{2+}, cosmetics can contain 700–30 000 parts per million.[24]

Though they are currently too costly, portable X-ray fluorescence equipment have recently been created to quickly assess the Hg^{2+} content of various objects.[25] New analytical techniques, such as atomic absorption spectrometry (AAS), electrochemical sensing, and inductively coupled plasma mass spectrometry (ICP-MS), have been developed recently for the detection of mercury ions.[26–28] One typical disadvantage of these methods is the need for costly and sophisticated equipment. However, molecular optical sensing makes it possible to monitor a particular analyte by attaching a selective optical signal transducer to a heavy element of detection.[29]

In recent years, rhodamine-based chemosensors have attracted a lot of interest among different chemosensor platforms.[30–32] Because of their remarkable optical qualities, high photoluminescence quantum yield, exceptional photo-irradiation stability, and capacity to change their fluorescence when interacting with metal ions, rhodamine dyes-which are well-known for their excellent fluorescence properties-have been extensively used in the design of chemosensors. Because these fluorescence enhancements are easily quantifiable, rhodamine-based probes are ideal for identifying hazardous metal ions.[33–39]

We have designed and synthesized a new (*E*)-2-hydroxy-3-methoxy-4-((4-nitrophenyl)diazenyl)benzaldehyde-condensed rhodamine hydrazone derivative (**L**) as a single chemosensor for sensing of Hg^{2+} in a mixed solvent C_2H_5OH–H_2O (4 : 1, v/v), as part of our ongoing project in search of the potential chemosensors for the hazardous metal ions.[40–43] Scheme 1 shows the synthesis's general layout. Through the chelation-enhanced fluorescence (CHEF) process[44] and inhibited PET, which were supported by various photophysical processes, the probe **L** demonstrates the "*turn on*" fluorescence property.[45] Using the sensing properties, we can build an INHIBIT molecular logic gate and used the suggested probe to analyze the environment. The experimental findings are well-correlated with theoretical results using density functional theory calculations.

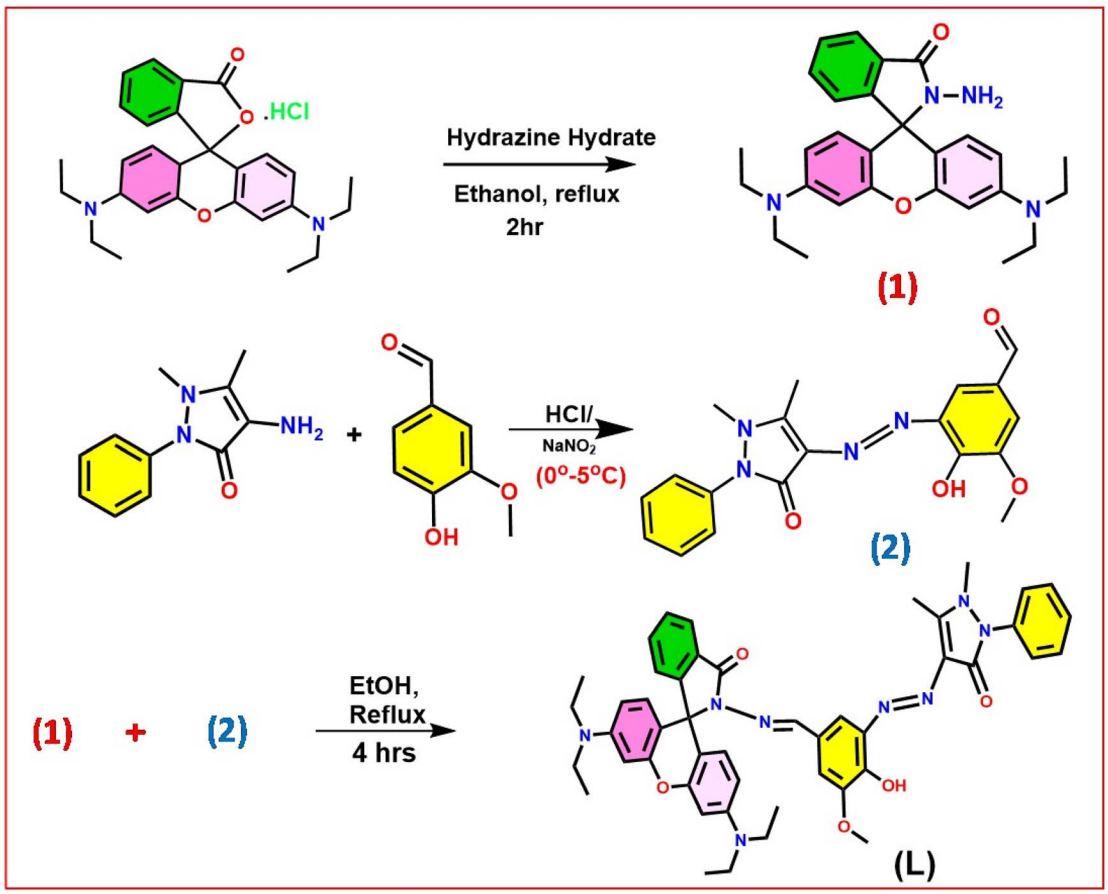

Scheme 1 Synthesis of the probe **L**.

2 Experimental

2.1 Materials and methods

Sigma-Aldrich provided the analytical-grade compounds, which included rhodamine B salt (99.0%), vanillin (99%), ampyrone (99%), and other metal salts and solvents. These were used without additional purification. The spectrum change of the chemosensor moiety was seen at a constant ligand concentration upon the addition of metal nitrate salts. Salts of metal perchlorate were purchased commercially. All of the metal salts and acquired compounds were purchased from Merck. It is necessary to start by using all of the salts (nitrate) that have been re-crystallized from water (Millipore). H_2O and C_2H_5OH–H_2O (4 : 1, v/v) solutions were prepared for cations (1×10^{-4} M) and receptor **L** (1×10^{-5} M), respectively.

2.2 Physical measurements

The melting points were determined using an X-4 digital melting-point device and were not modified. A Shimadzu UV 1800 spectrophotometer was used to record UV-visible spectra from a quartz cuvette with a route length of 10 mm. With an excitation wavelength of 500 nm, an XENO Flash (PTI) fluorescence spectrophotometer was used to acquire fluorescence spectra and relative fluorescence intensity. A PerkinElmer infrared spectrophotometer (Model: 883) was used to acquire infrared spectra (KBr pellet, 400–4000 cm^{-1}). A Bruckner 400 MHz instrument in DMSO-d_6 was used to get the ^1H NMR spectra, with TMS acting as the internal standard. ^1H–^1H coupling constants are given in hertz (Hz), and chemical shifts (δ) are given in parts per million (ppm). A digital pH meter (Merck) was adopted to measure the pH. Mass spectra were obtained using the Qtof Micro YA263 mass spectrometer.

2.3 Synthesis of rhodamine B hydrazide (1)

Xiang *et al.* (2007) and Thakur *et al.* (2023) explained the procedures employed in the synthesis of rhodamine B hydrazide.[46,47] 1.20 g (2.5 mmol) of rhodamine B (hydrochloride salt) was dissolved in 30 mL of ethanol within a 100-mL flask. Hydrazine hydrate (5 mmol, extra) (85%) was added dropwise simultaneously continuously swirling at room temperature. The reaction mixture was refluxed in an air steam bath for two hours with continuous stirring. Hazy purple was turned into vibrant orange after reflux. The subsequent cooling of reaction mixture under air pressure facilitated the removal of the solvent. A clear red solution was obtained by dissolving the 50 mL of 1 M HCl in the flask. Subsequently, 55 mL of 1.0 M sodium hydroxide was added gradually and stirring until the pH was reached 9.0. The precipitate was filtrate and rinsed three times with 15 mL of water. The reaction yielded 0.83 g of RBH (75%) with purity, resulting in a peach-colored solid followed by drying under infrared light. Crystallization with CH_3CN/H_2O was employed to enhance the purity of the product. The melting point of product was 176 °C.

2.4 Synthesis of azo dye [3-((1,5-dimethyl-3-oxo-2-phenyl-2,3-dihydro-1*H*-pyrazol-4-yl) diazinyl)-4-hydroxy-5-methoxybenzaldehyde] (2)

Azo compound was produced as described by Rao *et al.* and Bashandy *et al.*[48,49] 0.837 g of ampyrone (4.12 mmol) was dissolved in 2 mL of concentrated HCl, yielding a transparent green colour. This solution in the beaker was aggressively agitated in an ice-salt solution to maintain a temperature of 5 ° C. To achieve the desired frigid temperature, 0.284 g (4.12 mmol) of sodium nitrite solution was utilized. At this moment, the solution's color changed from green to light yellow. To the pale-yellow diazo solution at 5 °C, sodium hydroxide (0.165 g, 4.12 mmol), sodium carbonate (0.266 g, 2.51 mmol), and vanillin (0.627 g, 4.12 mmol) in 20 ml H_2O were added. After that, the mixture was allowed to stand at room temperature. The mixture was then filtered using a Whatman-41 filter paper, and the filtrate was treated with a 10% sodium chloride solution. The filtrate was solidified by adding water with a pH of 4. The orange-colored product was then vacuum-dried and confirmed by chromatography. We achieved 80% product yield, and the melting point of **2** was 110 °C.

2.5 Synthesis of the probe L (3)

Probe **L** was synthesized following the methodology outlined by Mabhai *et al.*,[50] with modifications involving a reflux reaction during the condensation of an aldehyde precursor with rhodamine B hydrazide (**1**) (Scheme 1). 20 mL of ethanol were employed to dissolve 0.536 g (1.175 mmol) of rhodamine B hydrazide and 0.430 g (1.175 mmol) of 3-((1,5-dimethyl-3-oxo-2-phenyl-2,3-dihydro-1*H*-pyrazol-4-yl)diazinyl)-4-hydroxy-5-methoxy benzal-dehyde (**2**). The mixture was subsequently heated while a $CaCl_2$ guard tube was positioned atop the condenser. The maroon solid was synthesized following four hours of refluxing. The mixture was subsequently cooled to room temperature, and during TLC monitoring, the reaction continued to develop. Heating in a water bath reduced the total volume of the suspension solution by one-third. Standard gravimetric filtering was performed. The successive washings with cold EtOH–Ether (1 : 1) produced the reddish-brown precipitate. A yield of 65% with a melting point of 210 °C was observed. Anal. Calc. for $C_{47}H_{48}N_8O_5$: C, 70.13; H, 6.01; N, 13.92. Found C, 70.25; H, 6.09; N, 14.01%. ^1H NMR [400 MHz, DMSO-d_6] δ (ppm): 8.72 (s, 1H, ArCH=N–), 7.87–7.80 (d, 1H, Ar–H), 7.64–7.50 (m, 2H, Ar–H), 7.44–7.32 (m, 4H, J = 6.4 H, Ar–H), 7.19–7.04 (m, 3H, J = 8.4 Hz, Ar–H), 6.77–6.74 (t, 1H, J = 8 Hz), 6.49–6.33 (m, 6H, xanthene-H, J = 8 Hz), 3.83 (s, 3H, O–CH_3), 3.31–3.30 (q, 8H, N–CH_2), 3.15 (s, 3H, N–CH_3), 2.10 (S, 3H, ArC=C–CH_3), 1.077 (S, 12H, –CH_3) (Fig. S1). ^{13}C NMR [100 MHz, DMSO-d_6] δ (ppm): 165.79, 160.48, 153.51, 153.14, 152.46, 152.33, 148.64, 129.84, 128.96, 128.82, 128.65, 128.13, 123.99, 122.98, 122.64, 112.49, 108.31, 106.10, 105.87, 97.94, 97.70, 65.71, 65.29, 56.07, 35.44 and 12.92 (Fig. S2). FTIR/cm^{-1} (KBr): 3975 (m, –OH), 1688 (s, C=O), 1610 (s, C=N), 1511 (s, N=N), 1309 (s, C=C), 823 (m), 748 (m), 687 (m), 626 (m) (Fig. S3). EI-MS: m/z 804.3714 (MH^+) (Fig. S4).

2.6 Association constant

The association constant for the formation of the complex [**L**-Hg^{2+}], were calculated by using the Benesi–Hildebrand (B–H) equation.

$$\frac{1}{A - A_0} = \frac{1}{[K(A_{max} - A_0)C]} + \frac{1}{(A_{max} - A_0)}$$

where, K is the association constant, which was calculated from the ratio of the slope and intercept of the linear plot, A_0 is the absorbance maxima of sensor **L**, A is the observed absorbance at that specific wavelength at different concentrations of the metal ion (C), A_{max} is the maximum absorbance value at λ_{max} = 556 nm (for M^{n+}) during titration by varying [C], and [C] is the concentration of the M^{n+} ion added during the titration studies. The quality of the linear fit of the B–H plot of $1/(A - A_0)$ *vs.* $1/[M^{n+}]$ for 1 : 1 complex formation verifies the binding stoichiometry between the chemosensor **L** and M^{n+}.

2.7 UV-visible sensing procedure

Ten milliliters of a 4/1 v/v ethanol–water solvent mixture were used to dissolve the probe **L** in a pH-7 HEPES ((4-(2-hydroxyethyl)piperazine-1-ethanesulfonic acid)) buffer solution. To get a final concentration of 10 mM, 30 mL of this were diluted to 3 mL using the solvent mixture. Separately, a solution was prepared in de-ionized water that contained the guest cation Hg^{2+} along with other tested cations in a concentration of 10 mM nitrate salts. Room temperature UV-Vis spectra were obtained after **L** was briefly combined with each of the other metal ions.

2.8 Fluorescence sensing procedure

Studies using fluorescence spectroscopy evaluated the receptors' ability to act as cation probes. Since the majority of the metal ions under study are extremely dangerous and have a detrimental effect on human health, all waste solutions containing heavy metal ions were recovered in order to prevent environmental pollution. To prepare 1×10^{-3} M stock solutions, the nitrate salts of the metal (Fe^{2+}, Cu^{2+}, Ni^{2+}, Cr^{2+}, Co^{2+}, Sn^{2+}, Hg^{2+}, Mn^{2+}, Pb^{2+}, Mg^{2+}, Al^{3+}, Fe^{3+}, Pd^{2+}, Cd^{2+}, Ag^{+} and Zn^{2+}) were dissolved in double distilled water. A 4/1 v/v ethanol–water solvent mixture was used to dissolve **L**. Titration experiments were carried out in a 1 cm quartz cuvette at room temperature. Following the addition of 3 mL of **L** solution to the quartz cell, the fluorescence spectra was recorded. To titrate it, the proper metal salt solution (1×10^{-6} M) was progressively added in little amounts (10 mL), and variations in fluorescence intensity were noted at room temperature. The sensitivity limits of **L** were assessed by adding varying concentrations of Hg^{2+}. A fluorescence spectrophotometer was used to analyze the mixtures in seconds after the addition of metal ions (λ_{ex} = 500 nm).

2.9 Density functional theory (DFT) calculations

Density functional theory (DFT) calculations for quantum mechanics/molecular mechanics (QM/MM) were performed using the DMol^3 module within Materials Studio 2020 employing the PWC exchange–correlation functional under the local density approximation (LDA).[51–53] Initially, the structure geometry was optimized. The calculations were spin-

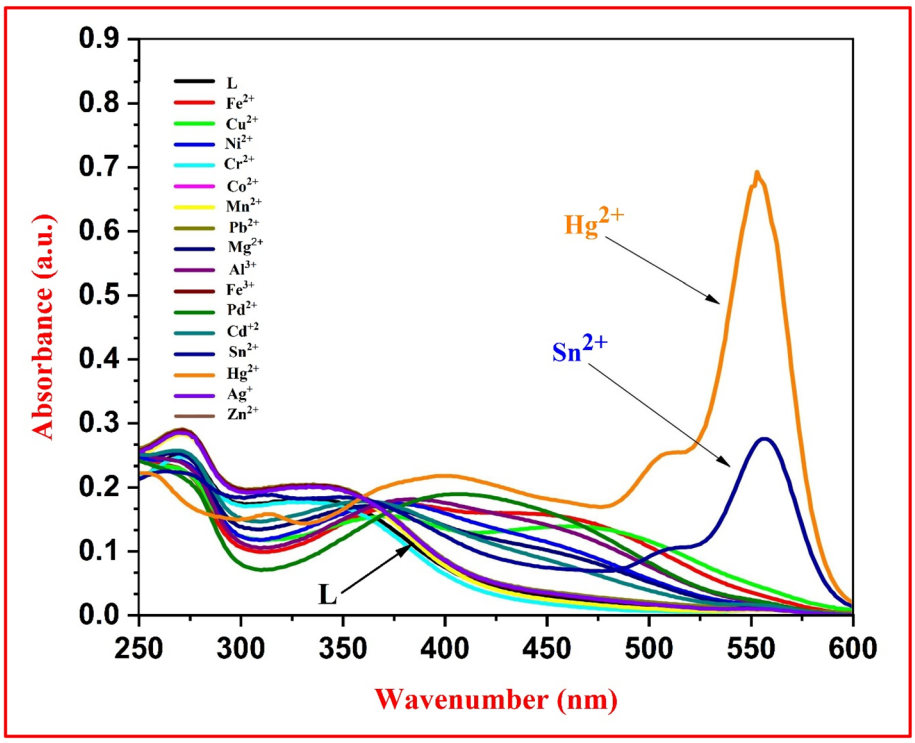

Fig. 1 UV-Vis spectra of **L** (40 μM) upon addition of various metal ions (Fe^{2+}, Cu^{2+}, Ni^{2+}, Cr^{2+}, Co^{2+}, Sn^{2+}, Hg^{2+}, Mn^{2+}, Pb^{2+}, Mg^{2+}, Al^{3+}, Fe^{3+}, Pd^{2+}, Cd^{2+}, Ag^{+} and Zn^{2+}) in a HEPES buffer [C_2H_5OH–H_2O (4 : 1,v/v) pH = 7.2] at 25 °C.

unrestricted, utilizing the DND basis set without pseudopotentials for all-electron calculations. Symmetry constraints were turned off and a medium integration grid was applied with a global energy cutoff of 3.3 Å. Fractional occupations were treated using thermal smearing with a width of 0.0050 hartree to ensure robust SCF convergence. The SCF density convergence tolerance was set with a charge mixing parameter of 0.2000, a maximum of 50 SCF iterations and Pulay DIIS (6 vectors) for enhanced convergence. Mulliken and Hirshfeld population analyses were performed to study charge distributions and electrostatic properties, including ESP fitting and electrostatic moments were calculated. Additional outputs included plots for the HOMO, LUMO, electron density and electrostatic potential. The grid for these calculated properties was defined with dimensions of 3 × 3 × 3 Å and a step size of 0.25 Å. The whole process was performed in Biovia Discovery Studio Client 4.1.[54]

3 Results and discussion

3.1 UV-visible spectroscopic studies

The UV-visible absorption spectra of a 40 μM probe solution in a quartz tube containing 2 mL EtOH–H_2O (4 : 1, v/v) pH = 7.2 using 20 μM HEPES buffer at 25 °C were recorded in order to verify the sensing capabilities of the chemosensor **L**. This was done by adding 100 μM stock solutions of various metal ions, such as Fe^{2+}, Cu^{2+}, Ni^{2+}, Cr^{2+}, Co^{2+}, Sn^{2+}, Hg^{2+}, Mn^{2+}, Pb^{2+}, Mg^{2+}, Al^{3+}, Fe^{3+}, Pd^{2+}, Cd^{2+}, Ag^{+} and Zn^{2+} Interestingly, no other metal cations changed the UV-visible spectral character of the probe **L**, with the exception of Hg^{2+} and Sn^{2+} ions. When Hg^{2+} and Sn^{2+} were added to probe **L**, strong bands appeared at λ_{max} = 505 nm and 556 nm, respectively, in the visible region of the absorption spectrum of **L** (Fig. 1). These bands were linked to instantaneous changes in the colour of the light reddish brown probe solutions to deep pink, which were easily visible to the unaided eye for direct recognition (Fig. 2 upper part). Under the UV-light the colour change is only seen in case of the addition of Hg^{2+} ions (Fig. 2 lower part). These new absorption spectral bands' appearance in the UV-visible spectrum's visible region showed that the complex formed by metal ion chelation caused the spirolactam ring to open, generating the conjugated xanthene framework.

To verify the probe's (**L**) reversible binding nature, UV-visible titrations of the probe **L** with Hg^{2+} and the resultant **L**-Hg^{2+} complex with Na_2EDTA were performed. The development and deepening of the pink colour, as well as the gradual enhancement of the absorption intensity of the absorption band at λ_{max} = 556 nm, were clearly observed when Hg^{2+} additions (0–75 μM) were made to probe **L** (40 μM) in EtOH–H_2O (4 : 1, v/v) pH = 7.2 using 20 μM HEPES buffer at 25 °C, as shown in Fig. 1. The UV-Vis titration experiment has been shown in the Fig. 3. But when a powerful chelating agent, Na_2EDTA (0–360 μM), was gradually added to the resultant **L**-Hg^{2+} complex solution, the strength of the aforementioned absorption band at λ_{max} = 556 nm immediately decreased, and the pink colour also vanished. The reversible binding nature of the probe was demonstrated by the regeneration of the free probe **L** through the demetallization of Hg^{2+} from the **L**-Hg^{2+} complex (Fig. 4).

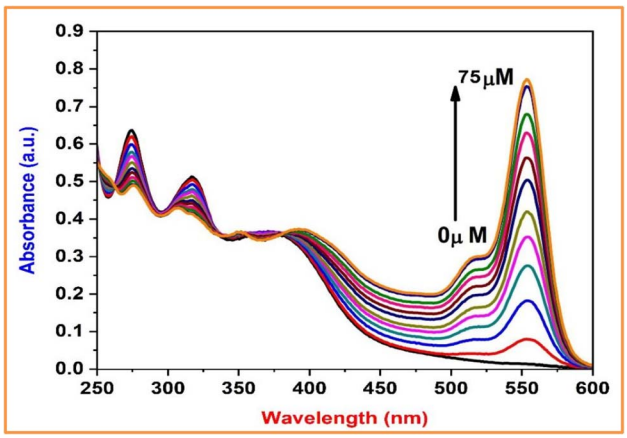

Fig. 3 UV-Vis spectral changes of L (40 μM) upon steady addition of Hg^{2+} ions in a HEPES buffer [50 μM, C_2H_5OH–H_2O (4 : 1, v/v, pH = 7.2)].

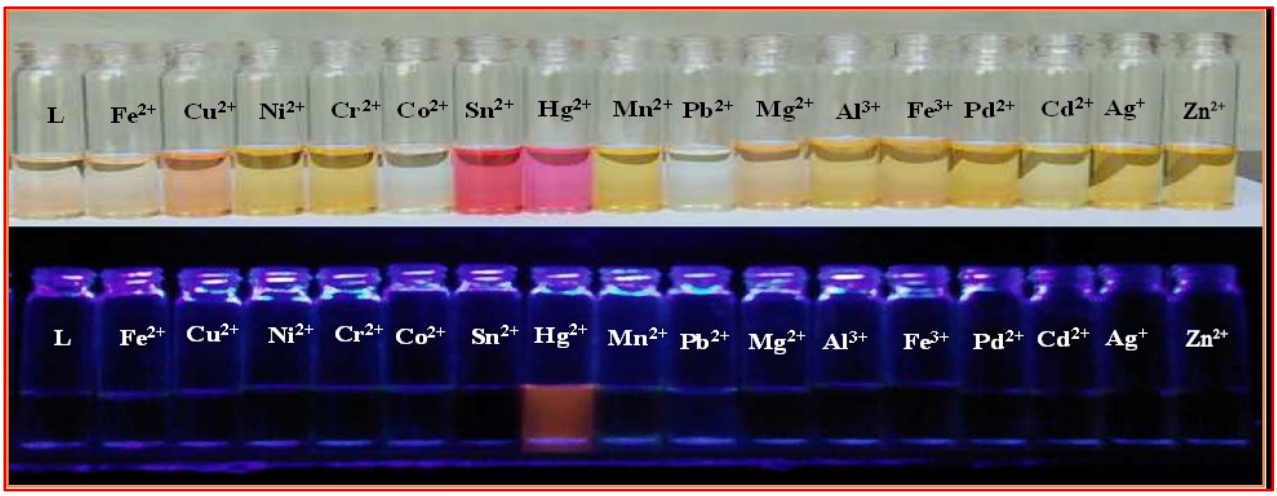

Fig. 2 Illustration of L and L + various metal ions: naked eye (upper part), under UV cabinet (lower part).

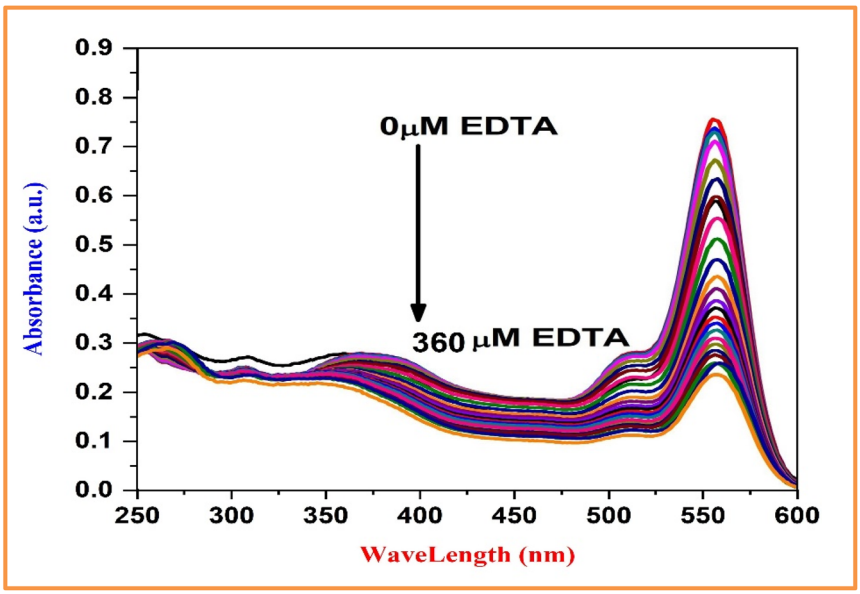

Fig. 4 UV-Vis spectral changes of Hg^{2+} complex of L upon addition of EDTA in C_2H_5OH–H_2O (4 : 1, v/v).

We then recorded UV-visible spectra of the probe **L** in the presence of Hg^{2+} (100 μM) mixed with other competing metal cations (100 μM), such as Fe^{2+}, Cu^{2+}, Ni^{2+}, Cr^{2+}, Co^{2+}, Sn^{2+}, Hg^{2+}, Mn^{2+}, Pb^{2+}, Mg^{2+}, Al^{3+}, Fe^{3+}, Pd^{2+}, Cd^{2+}, Ag^{+} and Zn^{2+} in order to examine the chemosensor **L**'s ability to recognize Hg^{2+} in the presence of other competing metal cations. We discovered that the presence of various metal cations had no effect on the absorbance intensity or band location of the **L**-Hg^{2+} complex (Fig. 5). This observation provides compelling evidence that the presence of other metal ions has no effect on the selectivity of this Hg^{2+} probe.

Furthermore, the Job's plot employing UV-visible titrations of the probe **L** and Hg^{2+} with a total concentration of 40 μM was used to gain a deeper understanding of the binding behaviour of the probe **L** with Hg^{2+}. The Job's plot analysis revealed that the 0.5 mole portion of Hg^{2+} had the maximum UV-visible absorption, suggesting a 1 : 1 stoichiometry for the **L**-Hg^{2+} complex (Fig. S5). Additional proof of a 1 : 1 stoichiometric complexation between the probe **L** and Hg^{2+} was found in the complex's ESI-MS spectra (Fig. S6), which showed a peak for [**L** + Hg^{2+} + $2NO_3$ + H_2O] at m/z = 1149.04.

Using 40 μM HEPES buffer at 25 °C, the detection limit was likewise determined by $3\sigma/m$ method[55] to be 1.01 μM in EtOH–H_2O (4 : 1, v/v) pH = 7.2 (Fig. 6). Any chemosensor's lower detection limit determines its likelihood for successful application. Our probe has a substantially lower limit of detection value than others, which increases its potential for application as an environmentally friendly chemosensor **L**.

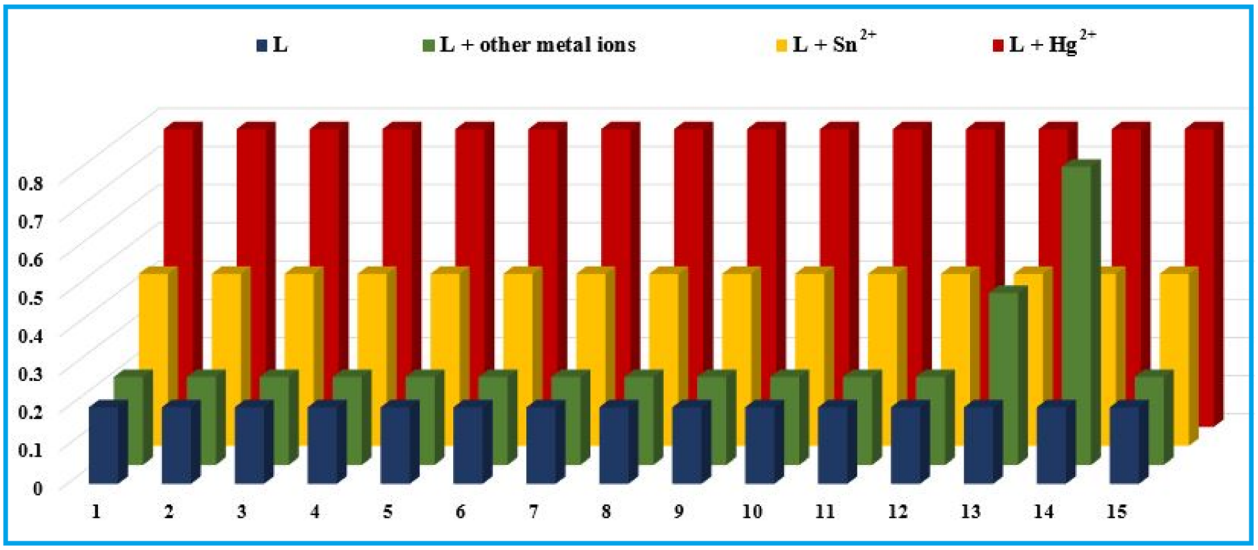

Fig. 5 Absorbance competitive experiment of L with other metal ions (where 1 = Fe^{2+}, 2 = Cu^{2+}, 3 = Ni^{2+}, 4 = Cr^{2+}, 5 = Co^{2+}, 6 = Sn^{2+}, 7 = Hg^{2+}, 8 = Mn^{2+}, 9 = Pb^{2+}, 10 = Mg^{2+}, 11 = Al^{3+}, 12 = Fe^{3+}, 13 = Pd^{2+}, 14 = Cd^{2+}, 15 = Ag^{+} and 16 = Zn^{2+}).

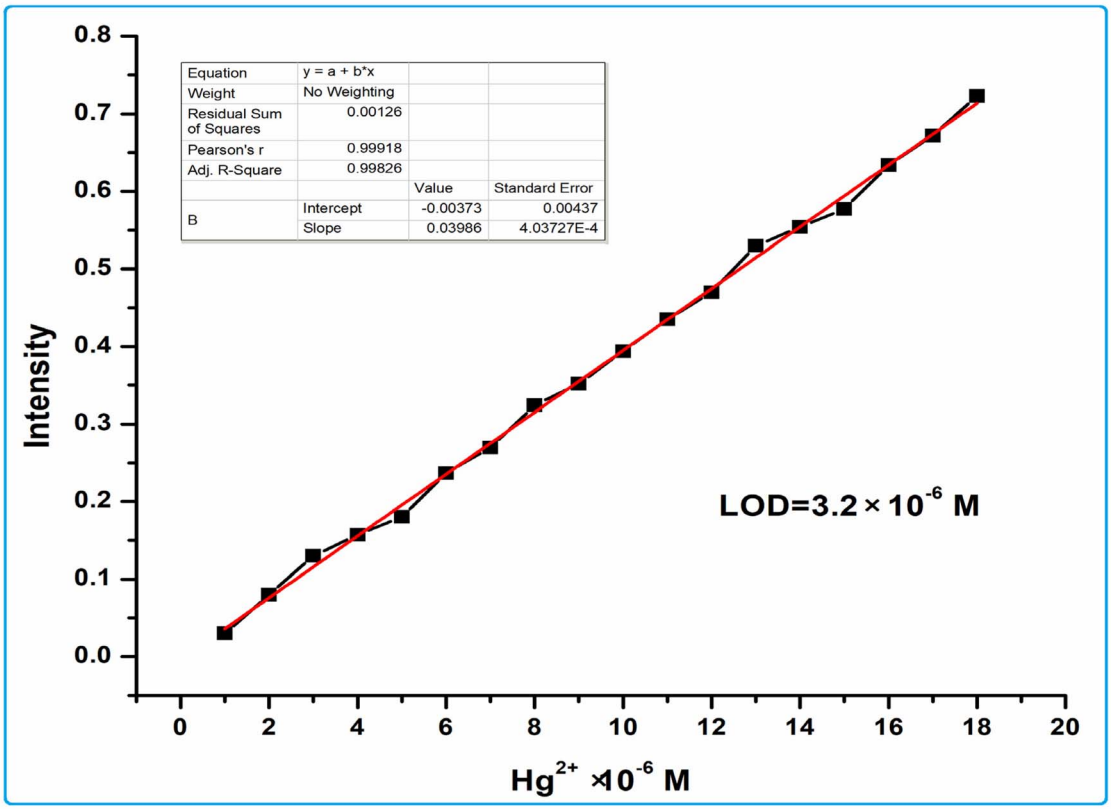

Fig. 6 Detection limit for Hg^{2+} from absorption titration in $C_2H_5OH–H_2O$ (4 : 1, v/v).

3.2 Fluorescence spectroscopic studies

Fluorescence spectroscopic investigations were also used to investigate the sensing behaviour of the chemosensor **L**. According to the experimental results, the probe **L** itself did not exhibit any discernible emission band above $\lambda_{max} = 575$ nm when excited at $\lambda_{ex} = 500$ nm and in the presence of various metal ions, including Fe^{2+}, Cu^{2+}, Ni^{2+}, Cr^{2+}, Co^{2+}, Mn^{2+}, Pb^{2+}, Mg^{2+}, Al^{3+}, Fe^{3+}, Pd^{2+}, Cd^{2+} and Ag^{+}, in EtOH–H_2O (4 : 1, v/v), pH = 7.2. The solution (20 μM, **L**) exhibited a very weak emission band at $\lambda_{max} = 575$ nm. However, because CHEF occurred and the PET process was hindered, a notable increase in fluorescence intensity was observed at $\lambda_{max} = 584$ nm (Fig. 7a) only in the presence of Hg^{2+} (quantum yield $\Phi = 0.46$). Column plot for the emission spectral intensity of **L** (50 μM) upon addition of different metal ions has been provided in Fig. 7b.

L is a non-fluorescent molecule as the lone pair (lp) from the -NEt_2 group migrates to the azobenzene moiety. However, this lp in **L** becomes inaccessible when it binds to the Hg^{2+} ion in the Hg^{2+}-complex of **L**, rendering the **L** luminous in areas where the PET process is hindered. The reason for this high affinity for Hg^{2+} is that its bivalency have a greater binding energy, tiny ionic radius and high charge density, makes it hard acid. According to the well-known HSAB (hard and soft acids and bases) principle, the ligand (**L**) with the binding site with N and O has a strong tendency to chelate with Hg^{2+}. For this reason, probes with N and O as donor sites are frequently used for the sensing of Hg^{2+} ions.[56–58] Fluorescence enhancement (58 fold) in **L** upon the addition of Hg^{2+} is mainly caused by the metal-ion-induced ring opening of the spirolactam moiety, accompanied by CHEF and PET inhibition, leading to a strong "off–on" fluorescence response.

Additionally, when 2.5 equivalents of Hg^{2+} were added to the probe solution, the colour changed significantly from light reddish brown to an intense orange fluorescence under a UV lamp with a long wave length (360 nm). This indicated that **L** exhibited Hg^{2+} selective "*turn-on*" fluorescence signalling activity [Fig. 2]. Using the fluorimetric titration method, the reversible behaviour of **L** was also investigated. The experimental observation showed that the emission intensity of the emission band around $\lambda_{max} = 584$ nm in the emission spectrum of the probe **L** gradually increased with the gradual addition of Hg^{2+} to the probe solution. This emission intensity gradually decreased with successive excess additions of Na_2EDTA [Fig. 8 and 9]. Our probe's potential as a selective fluorescence "on–off" probe for Hg^{2+} was once again validated by these data. By comparing the IR and ^{13}C NMR spectra of the free probe **L** and **L**-Hg^{2+} complex, we have validated our suggested mechanism of **L**-Hg^{2+} complex formation. The **L**-Hg^{2+} compound and the free probe had carbonyl stretching frequencies of 1642 cm^{-1} and 1688 cm^{-1}, respectively, for the spirolactam ring. This shifting (about 46 cm^{-1}) is indicative of the spirolactam ring opening phenomenon, in which carbonyl oxygen forms a bond with the Hg^{2+} ion (Fig. S7).[59] When Hg^{2+} was added, the tertiary carbon signal that had occurred at $\delta = 65.27$ ppm vanished and a new signal appeared at $\delta = 133.04$ ppm, confirming the spirolactam

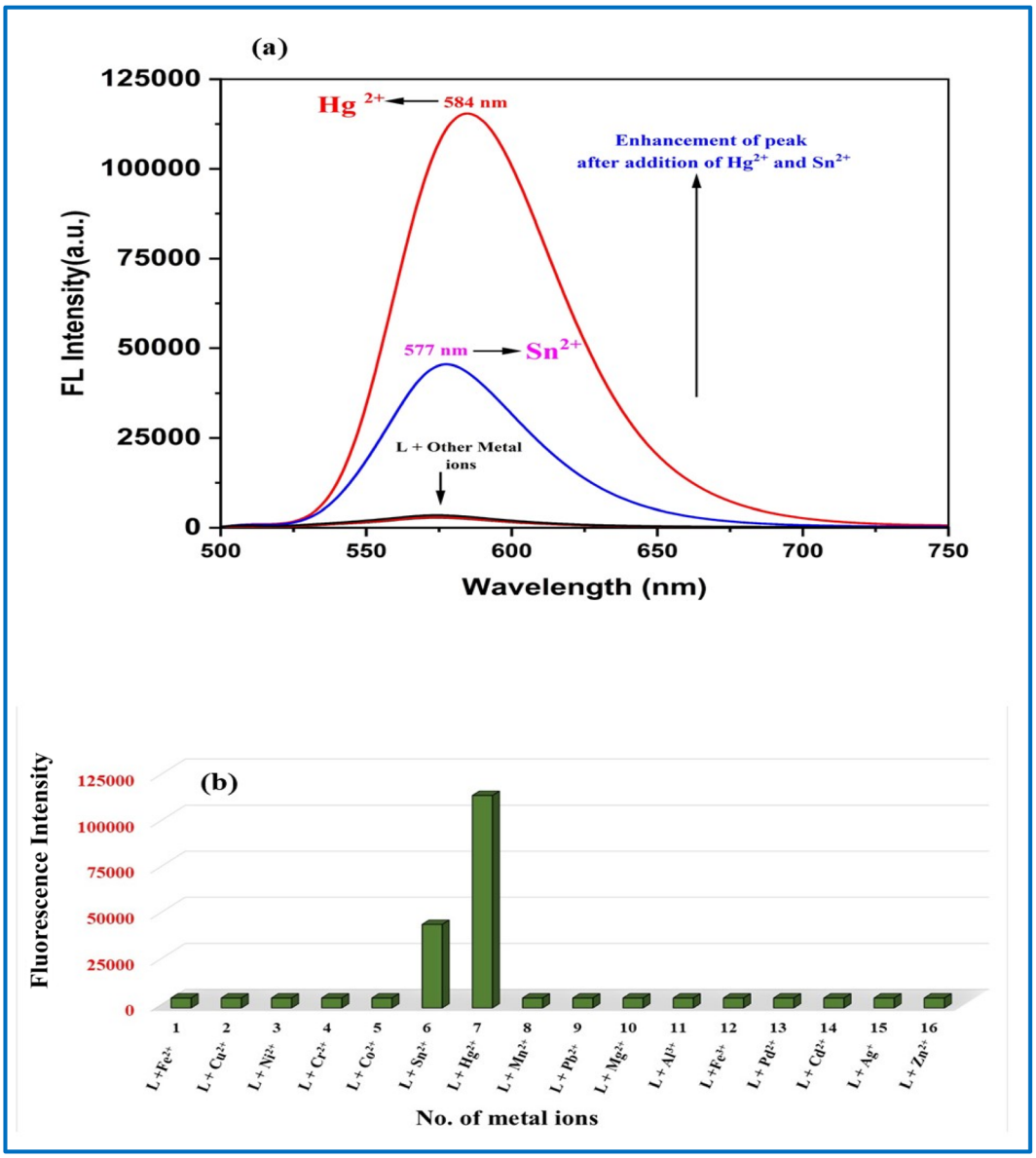

Fig. 7 (a) Emission spectral nature of L (20 μM) upon addition of various metal ions (Fe^{2+}, Cu^{2+}, Ni^{2+}, Cr^{2+}, Co^{2+}, Sn^{2+}, Hg^{2+}, Mn^{2+}, Pb^{2+}, Mg^{2+}, Al^{3+}, Fe^{3+}, Pd^{2+}, Cd^{2+}, Ag^{+} and Zn^{2+}) in a HEPES buffer (b) column plot for the emission spectral intensity of L (50 μM) upon addition of different metal ions.

ring opening process (Fig. S8).[60] This is explained by the fact that when rhodamine binds to the Hg^{2+} ion, the sp^3 spiro carbon changes into a sp^2 carbon.

We then recorded the fluorescence spectra of probe **L** with Hg^{2+} (100 μM) mixed with other competing metal cations (100 mM), such as Fe^{2+}, Cu^{2+}, Ni^{2+}, Cr^{2+}, Co^{2+}, Sn^{2+}, Mn^{2+}, Pb^{2+}, Mg^{2+}, Al^{3+}, Fe^{3+}, Pd^{2+}, Cd^{2+}, Ag^{+} and Zn^{2+} as illustrated in Fig. 10, to examine the recognition ability of **L** towards Hg^{2+} in the presence of other competing metal cations. Based on this, we discovered that the absorbance intensity and the band position of the **L**-Hg^{2+} complex remained unchanged in the presence of other cations. This observation provides compelling evidence that the presence of other cations has no effect on the selectivity of this Hg^{2+} probe.

The Benesi–Hildebrand plot of the emission titration data showed a linear curve based on the 1 : 1 binding stoichiometry, and the association constant (K_a) was determined to be 1.48×10^3 M (Fig. S9). Using 40 μM HEPES buffer at 25 °C, the detection limit from fluorescence data was determined by 3σ/m method[55] to be 1.2 μM in EtOH–H_2O (4 : 1, v/v) pH = 7.2 (Fig. 11).

3.3 Proposed sensing mechanism

Fluorometric and colorimetric titration of Hg^{2+} ions were carried out using a solution of **L** in an EtOH–water (4 : 1, v/v) buffer (10 mM, HEPES, pH 7.2) in order to further examine the sensing performance of the chemosensor. Scheme 2 and Fig. 1 illustrate how the fluorescent and colorimetric properties

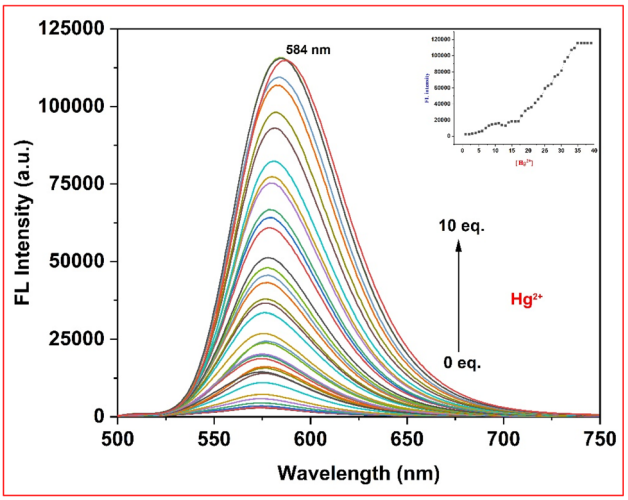

Fig. 8 (a) Changes in the emission spectrum of L (40 μM) at 25 °C after the addition of the Hg^{2+} ion in a HEPES buffer [50 μM, C_2H_5OH–H_2O (4 : 1, v/v, pH = 7.2)] [Hg^{2+}] = 0–10 eq. (b) Inset: 584 nm intensity *vs.* the quantity of equivalent Hg^{2+} added.

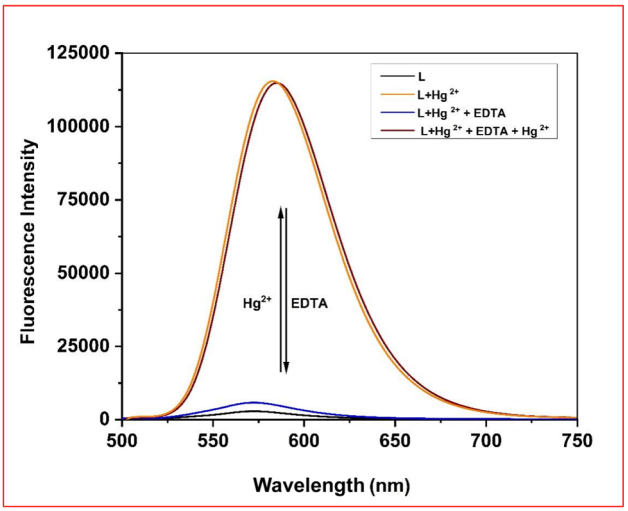

Fig. 9 Hg^{2+} complex of L (40 μM) emission spectrum changes when EDTA is added in a HEPES buffer solution [50 μM, C_2H_5OH–H_2O (4 : 1, v/v, pH = 7.2)] at 25 °C. EDTA = 0–10 eq.

of rhodamine emerged when Hg^{2+} was added to the bright reddish brown solution of **L**. This suggests that the amide group's oxygen atom on chemosensor **L** is crucial to the binding process with Hg^{2+}. The structural alteration of **L** from spirolactam (non-fluorescent) to ring-opened (fluorescent) form may also be connected to these modifications because of its complexation behaviour with Hg^{2+}.[61–63]

3.4 Effect of pH

Furthermore, the ideal pH values for the effective use of the fluorescent probe **L** and **L**-Hg^{2+} combination were examined. The effects of pH on the probe's fluorescence intensity were assessed for this experiment in the presence and absence of Hg^{2+} in an EtOH–water (4 : 1, v/v) buffer (10 mM, HEPES, pH 7.2), as shown in Fig. 12. It is commonly known that rhodamine-based spirolactam fluorescence probes often react to the Hg^{2+} ion in a pH-dependent manner. In line with numerous documented rhodamine spirolactam-based fluorescent chemosensors, it was discovered that the **L**-Hg^{2+} complex's fluorescence intensity dropped under acidic (pH = 6) conditions. Furthermore, no significant findings were found regarding the emission intensity of free **L** across the broad pH range of 2 to 12. Nonetheless, there was a noticeable variation in fluorescence intensity between pH = 6 to pH = 12 in the presence of Hg^{2+}. The experimental findings showed that the fluorescent chemosensor **L** may be utilised for high-selectivity Hg^{2+} ion detection at physiological pH levels.

3.5 Density functional theory (DFT) calculations

Initially, the geometry optimization was performed for the ligand (**L**) and its complex with Hg^{2+} (**L** + Hg^{2+}). The optimized structures with the electron density distributions were showed in Fig. 13.

The results reveal notable differences in the energy parameters of the ligand (**L**) and its complex with Hg^{2+} (**L** + Hg^{2+}). The bond energy increased from 2.4463 eV to 4.5441 eV upon complexation, indicating stronger interactions in the complex. The dihedral energy decreased slightly from 30.631 to 27.6544, suggesting a conformational change. The van der Waals energy became more negative, shifting from −17.2254 eV to −18.4642 eV, reflecting enhanced dispersion interactions in the complex. Electrostatic energy also changed significantly, from 5.7381 eV to −15.9831 eV, highlighting stronger electrostatic stabilization upon binding. Total energy shifted drastically from −2611.84 for the ligand to −21652.2 for the complex, indicating a major stabilization effect due to complexation. The binding energy also became more negative, changing from −22.3614 to −25.0361, confirming the favorable binding of Hg^{2+}. Finally, the dipole moment magnitude decreased from 5.31855 to 3.3996, indicating a redistribution of charge in the complex. The different energy parameters were reported in Table 1.

The DFT calculations for the electronic properties reveal important insights into the frontier molecular orbitals (HOMO and LUMO) and the band gap energy, which are critical for understanding the reactivity and stability of the ligand (**L**) and its complex with Hg^{2+} (**L** + Hg^{2+}). The HOMO energy, representing the highest occupied molecular orbital, increased from −0.1600 for the free ligand to −0.1367 for the **L**-Hg^{2+} complex. This increase (becoming less negative) suggests a reduction in the ionization potential and an enhancement of the electron-donating ability of the system upon complexation. Similarly, the LUMO energy, which corresponds to the lowest unoccupied molecular orbital, also increased from −0.1276 for the ligand to −0.1074 for the complex. The rise in the LUMO energy indicates a decrease in the system's electron affinity and implies that the complex is less susceptible to accepting electrons compared to the free ligand. The band gap energy, defined as the energy difference between the HOMO and LUMO, decreased slightly from 0.0323 for the ligand to 0.0293 for the complex. This

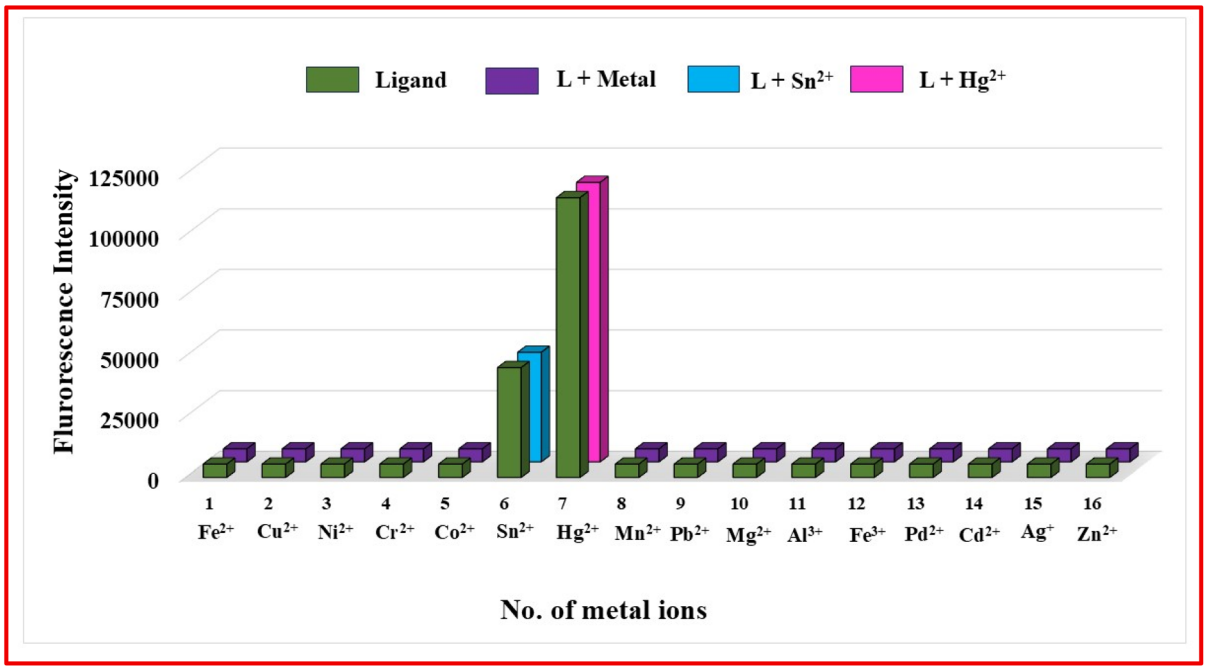

Fig. 10 Fluorescence intensity of L (40 μM) at 25 °C in a HEPES buffer [50 μM, $C_2H_5OH–H_2O$ (4 : 1), (v/v), pH 7.2] with different metal cations present. The fluorescence intensities of probe L in the presence of the relevant metal cations are shown by the green bars. purple, blue and pink bars represent the change of fluorescence intensity that occurred upon subsequent addition of Hg^{2+}, Sn^{2+} and other ion to the above-mentioned solution. λ_{ex} = 500 nm and λ_{em} = 577 (for Sn^{2+}) and 584 nm (for Hg^{2+}).

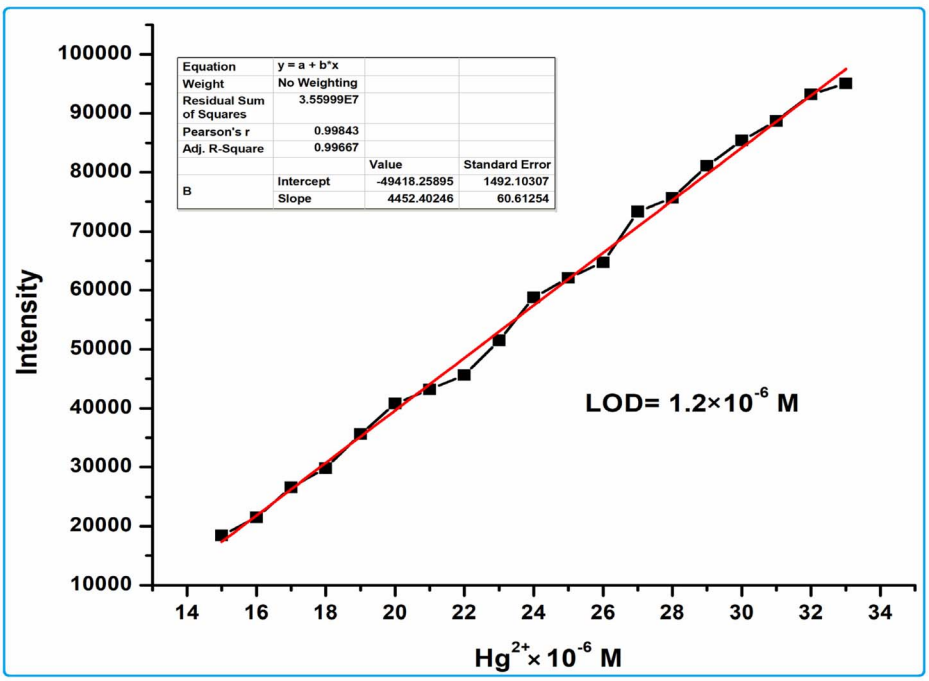

Fig. 11 Detection limit for Hg^{2+} from absorption titration in $C_2H_5OH–H_2O$ (4 : 1).

reduction in the band gap energy suggests a slight increase in the chemical reactivity of the system after binding with Hg^{2+}. The HOMO and LUMO orbitals and energies were showed in Fig. 14. Overall, the changes in the HOMO, LUMO, and band gap energies highlight the significant influence of Hg^{2+} binding on the electronic structure of the ligand, indicating enhanced stabilization and altered electronic behavior in the resulting complex.

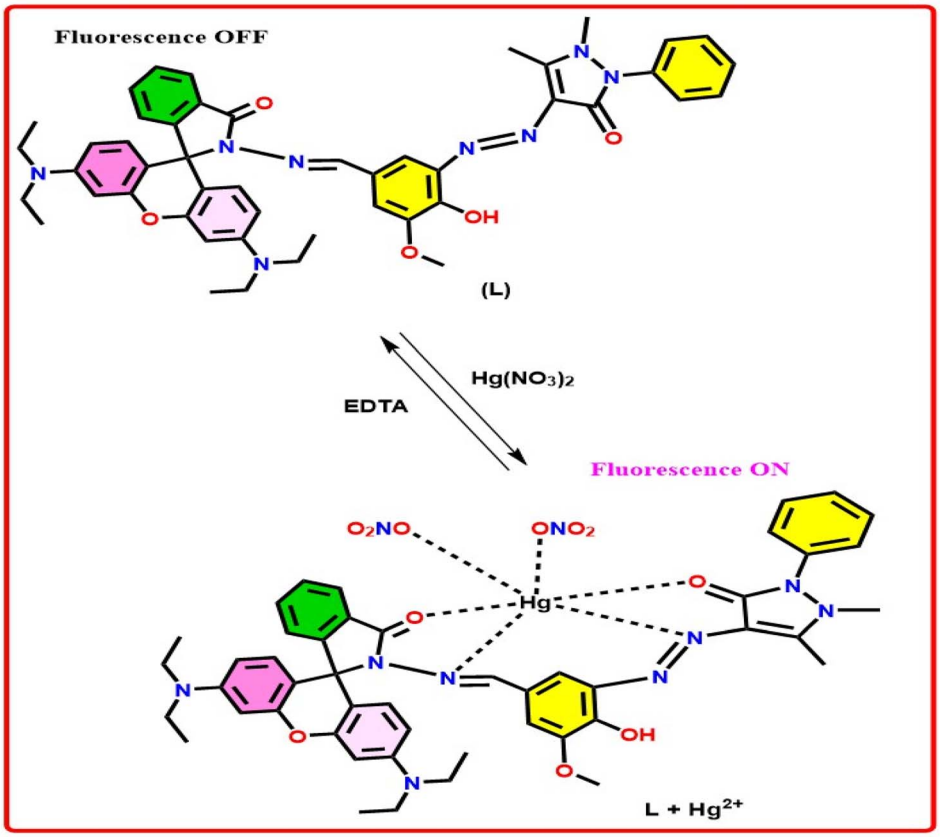

Scheme 2 Proposed sensing mechanism of L for Hg^{2+}.

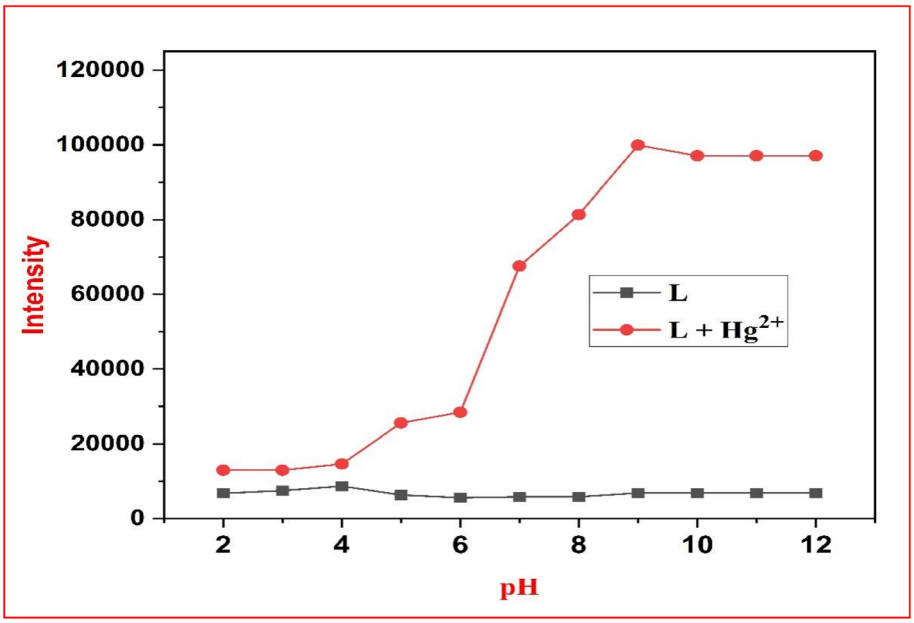

Fig. 12 pH effects with and without the Hg^{2+} ion [50 μM C_2H_5OH–H_2O (4 : 1,v/v, pH = 7.2)] excitation wave length = 500 nm and emission maxima wavelength of 584 nm at 25 °C.

The atomic charge analysis for ligand (**L**) using Mulliken, ESP-fitted and Hirshfeld methods highlights the variations in charge distributions and electrostatic properties across different atoms of ligand (**L**). Nitrogen atoms generally show slight negative charges in all methods, with Mulliken charges being slightly more negative than those from Hirshfeld and ESP

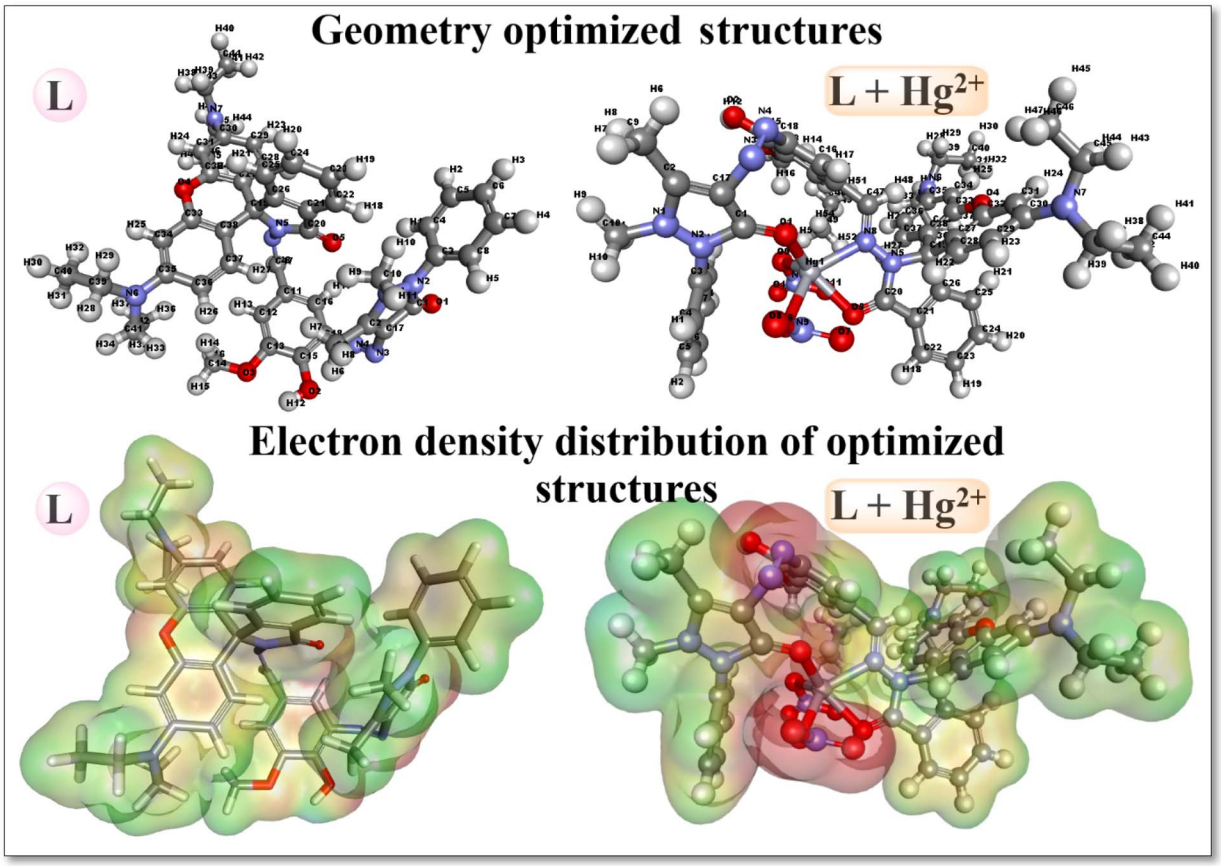

Fig. 13 Geometry optimized structures of L and L + Hg^{2+} with the electron density distributions.

Table 1 The different energy parameters obtain by DFT calculations

Name	L	L + Hg^{2+}
Bond energy	2.4463	4.5441
Dihedral energy	30.631	27.6544
Van der Waals energy	−17.2254	−18.4642
Electrostatic energy	5.7381	−15.9831
Total energy	−2611.84	−21652.2
Binding energy	−22.3614	−25.0361
HOMO energy	−0.1600	−0.1367
LUMO energy	−0.1276	−0.1074
Band gap energy	0.0323	0.0293
Dipole Mag	5.31855	3.3996

fitting. Carbon atoms exhibit a mix of positive and negative charges with their charges strongly influenced by their bonding environment as seen from significant variations between the methods. Oxygen atoms consistently carry negative charges with the most negative charges observed in the Mulliken method, indicating their higher electronegativity and role in electron density distribution. Hydrogen atoms display positive charges across all methods with ESP-fitted charges slightly higher than those from Mulliken and Hirshfeld, reflecting their participation in polar bonds. The analysis of atomic charges for **L**-Hg^{2+} complex using Mulliken and ESP fitting methods reveals a detailed picture of the molecule's charge distribution and electrostatic properties. Nitrogen and oxygen atoms carry significant negative charges due to their high electronegativity with ESP-fitted charges showing stronger polarization compared to Mulliken charges. Carbon atoms exhibit varying charges based on their bonding environment, with some acting as electron-rich centers and others as electron-deficient. The Hg atom displays a substantial positive charge highlighting its role as an electron-deficient site likely influencing molecular interactions. ESP-fitted charges provide a more accurate representation of electrostatic properties, while Mulliken charges offer a simpler, less polarized view. These results underscore the importance of polar regions and charge distribution in determining the molecule's reactivity and interaction potential. The plots for charges distribution for ligand (**L**) and ligand-Hg^{2+} (**L**-Hg^{2+}) complex was highlighted in Fig. 15 and reported in Tables TS1 and TS2 respectively.

4 Application

4.1 Molecular logic gate

The Schiff base chemosensor designed for the selective detection of Hg^{2+} ions exhibits molecular logic behavior that can be interpreted through an INHIBIT logic gate model. This chemosensor displays a significant "*turn-on*" fluorescence response at 585 nm upon binding with Hg^{2+}, due to enhanced

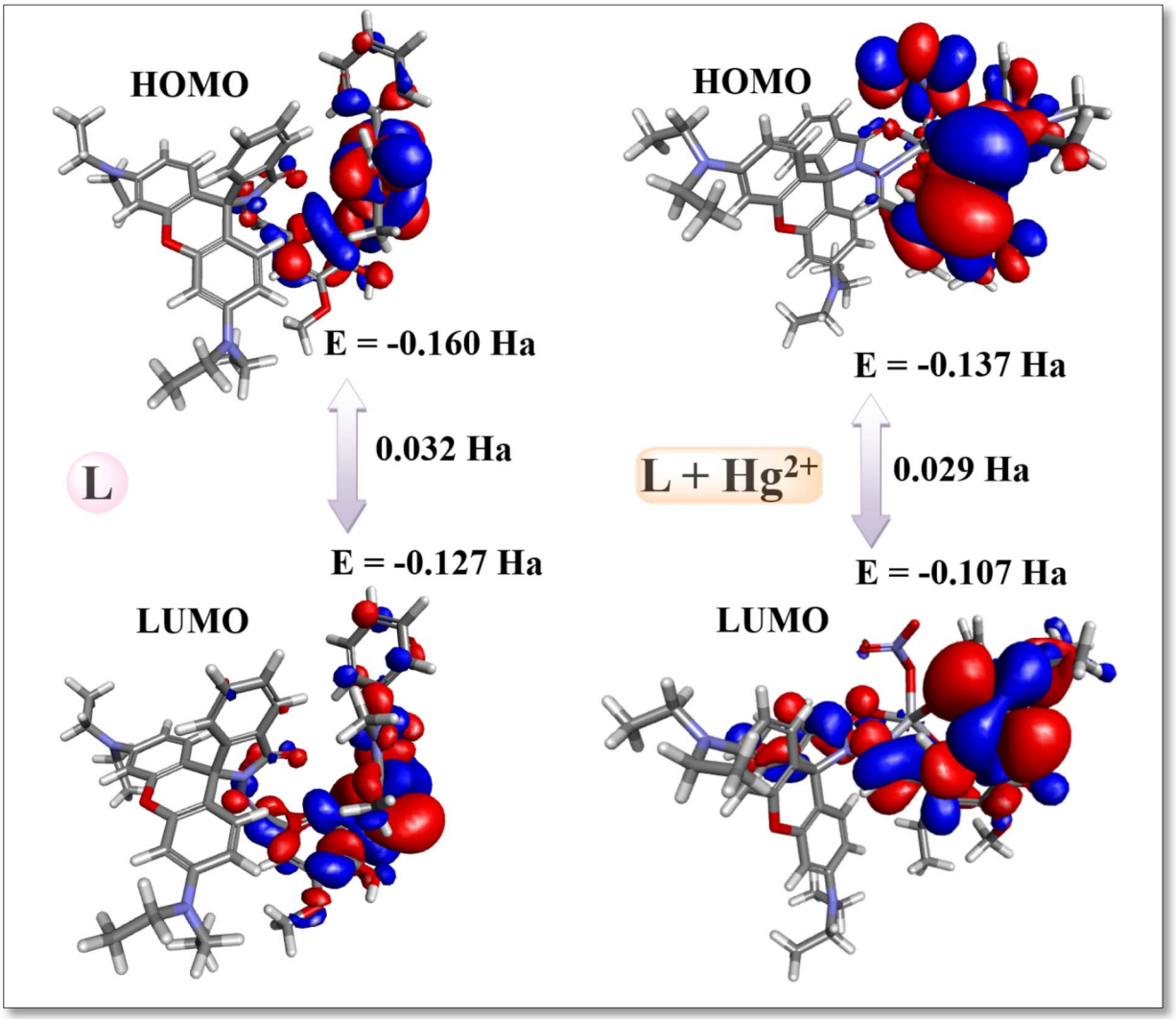

Fig. 14 HOMO and LUMO orbitals and along with their energies in L and L + Hg^{2+}.

intramolecular charge transfer (ICT) or conformational rigidification upon complex formation. In this molecular system, two chemical species are used as logic inputs: Hg^{2+} (input A) and EDTA (input B), while the output is the observed fluorescence intensity at 585 nm. When Hg^{2+} is introduced alone ($A = 1$, $B = 0$), it coordinates with the Schiff base moiety, triggering a marked increase in fluorescence intensity (output = 1), indicating the presence of the analyte. However, when EDTA is subsequently added ($A = 1$, $B = 1$), it acts as a competitive chelating agent, preferentially binding Hg^{2+} and thereby displacing it from the Schiff base binding site. This leads to quenching of the fluorescence signal (output = 0), effectively reversing the fluorescence response. In the absence of Hg^{2+} ($A = 0$), no fluorescence enhancement is observed regardless of the presence ($B = 1$) or absence ($B = 0$) of EDTA, as there is no metal ion available to form a complex with the probe. This logic behavior conforms to an INHIBIT gate, where fluorescence (ON state) is produced only when Hg^{2+} is present and EDTA is absent (Fig. 16). The reversibility of the system also allows for potential re-usability and dynamic control, making this chemosensor a promising candidate for the development of intelligent molecular logic circuits and reusable sensing platforms for toxic heavy metal ions.

4.2 Water sample analysis

To assess the practical feasibility of the synthesized ligand as an **L** for mercury ion detection, recovery experiments were performed in real water samples (tap water, pond water, and distilled water), each spiked with 5 μM of Hg^{2+}. The observed recovery percentages and associated standard deviations are presented in Table 2. The tap water samples showed a recovery of 98.10 ± 0.70%, indicating that the ligand retained high sensitivity and accuracy even in the presence of common ions and minor organic contaminants. In pond water, a slightly elevated recovery of 100.47 ± 1.72% was observed, which could be attributed to mild matrix interference typical of natural aquatic environments. Distilled water, used as a blank matrix, demonstrated a recovery of 97.00 ± 1.00%, confirming the **L**

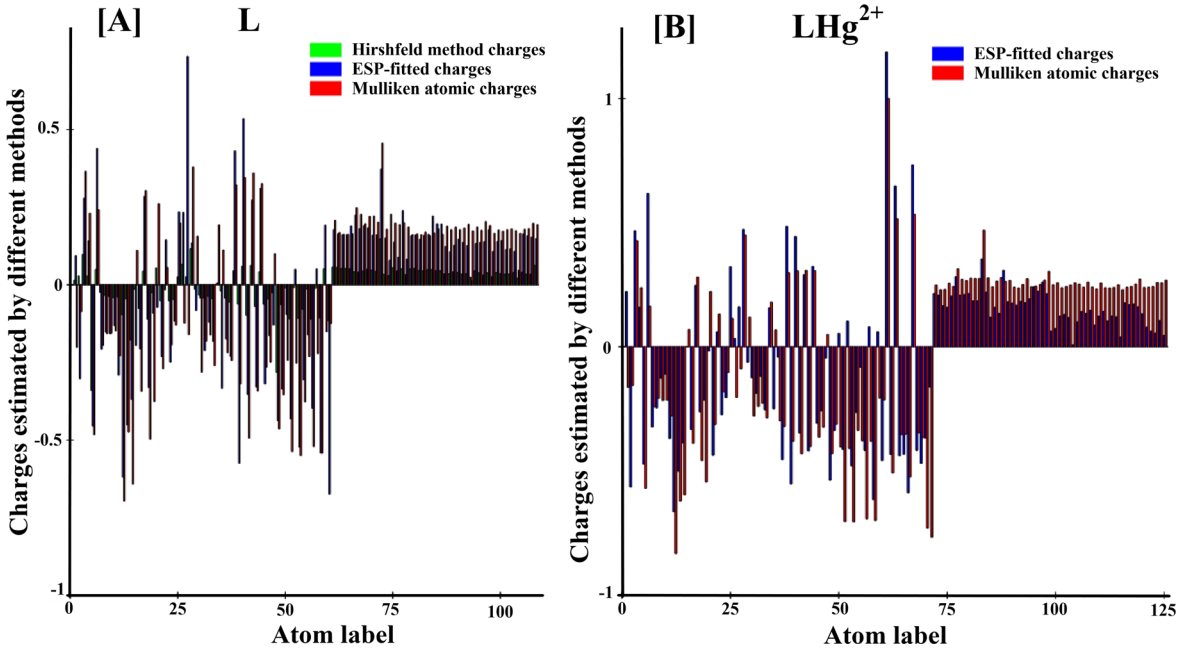

Fig. 15 Charges distribution for ligand (A) (L) and (B) ligand-Hg^{2+} (L-Hg^{2+}) complex.

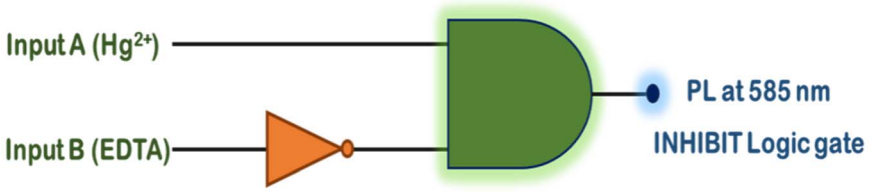

Input A (Hg^{2+})	Input B (EDTA)	Output (Fluorescence at 585 nm)	Logic
0	0	0	OFF
1	0	1	ON
0	1	0	OFF
1	1	0	OFF

Fig. 16 Molecular logic circuits and truth table, based on Hg^{2+} and EDTA for L.

Table 2 Determination of Hg^{2+} ion in different water samples by L

Sample	Spike (μM)	Recovery (μM)	Recovery (%) ±SD
Tap water	5	4.9, 4.95, 4.87	98.1 ± 0.7
Pond water	5	5, 5.12, 4.95	100.47 ± 1.72
Distilled water	5	4.8, 4.85, 4.9	97 ± 1

reliability under ideal, interference-free conditions. These findings highlight that the free ligand effectively detects Hg^{2+} with high accuracy and acceptable precision across various water samples. The consistent performance in both natural and laboratory-grade water matrices underscores the ligand's potential utility in environmental monitoring and field-deployable mercury sensing applications.

5 Conclusion

In conclusion, we have reported a rhodamine and functionalised azobenzene condensed novel chemosensor **L** that exhibits a notable shift in colorimetric and fluorometric response upon binding with Hg^{2+}. When Hg^{2+} is added, the colour changes from light reddish-brown to pink because of the PET inhibition

and CHEF processes. The 1 : 1 binding mechanism of metal with chemosensor, **L** is supported by the absorption and fluorometric measurements of Hg^{2+} with a high binding constant, titration profiles, and very low level of detection limits (7.9×10^{-6} M colorimetrically and 1.25×10^{-6} M fluorometrically). The sensing mechanism has been confirmed by FTIR, ^{13}C-NMR, ESI-mass spectra, Job's plot analysis and DFT studies. Furthermore, the receptor **L** can function in a broad pH range of 6–12, including physiological pH, and can be effectively used for real sample analysis and the building of an INHIBIT type logic gate. We believe that this chemosensor **L** is a promising probe for Hg^{2+} detection with the naked eye because of its remarkable selectivity and reversibility to Hg^{2+}.

Author contributions

Pradeep Sahu: conceptualization, methodology, investigation. Amit Kumar Chaturwed: methodology, formal analysis. Ashok Raj Patel: formal analysis. Vanshika Sharma: conceptualization and writing. Balaji Wamanrao Matore: theoretical calculations. Jagadish Singh: validation, DFT calculation. Partha Pratim Roy: DFT calculation and writing. Abhilash Pandey: visualization, Milan Hait: writing the manuscript and supervision. Goutam Kumar Patra: writing the manuscript, editing and supervision.

Conflicts of interest

Authors declare no conflicts of interest.

Data availability

Data will be made available on request after publication.

Fig. S1–S9 and Tables TS1 and TS2. See DOI: **https://doi.org/10.1039/d5ra03890a**.

Acknowledgements

G. K. P would like to thank the Department of Science and Technology (SR/FST/CSI-264/2014 and EMR/2017/0001789) and Department of Biotechnology, Government of India, New Delhi for financial support.

References

1 M. Kampa and E. Castanas, *Environ. Pollut.*, 2008, **151**, 362–367.
2 G. T. Miller and S. Spoolman, *Environmental Science*, National Geographics, Cengage Publishers, 16th edn, 2012.
3 Y. F. Chen, F. Wu, P. L. Li, Z. Q. Lyu, L. Liu, M. B. Lyu, F. L. Wang and C. H. Lai, *J. Anim. Sci.*, 2016, **94**, 5295–5307.
4 A. K. Verma, P. R. Rout, E. Lee, P. Bhunia, J. Bae, R. Y. Surampalli, T. C. Zhang, R. D. Tyagi, P. Lin and Y. Chen, *Biodiversity and Sustainability*, Wiley, 2010.
5 N. Suh, T. Honda, H. J. Finlay, A. Barchowsky, C. Williams, N. E. Benoit, Q. W. Xie, C. Nathan, G. W. Gribble and M. B. Sporn, *Cancer Res.*, 1998, **58**, 717–723.
6 K. A. Wade-Benzoni, M. H. Bazerman and C. Buisseret, in *A Senior-Level Dialogue on Climate Change*, ed. A. J. Hoffman, The New Lexington Press, San Francisco, 1998, pp. 78–84.
7 M. M. Ali, K. West, J. L. Teich, S. Lynch, R. Mutter and J. Dubenitz, *J. Sch. Health*, 2019, **89**, 393–401, DOI: **10.1111/josh.12753**.
8 N. B. Saidon, R. Szabó, P. Budai and J. Lehel, *Environ. Pollut.*, 2024, **340**, 122815.
9 R. A. Wuana and F. E. Okieimen, *ISRN Ecol.*, 2011, 402647, DOI: **10.5402/2011/402647**.
10 C. Garbisu and I. Alkorta, *Bioresour. Technol.*, 2001, **77**, 229–236.
11 E. M. Nolan and S. J. Lippard, *Chem. Rev.*, 2008, **108**, 3443–3480, DOI: **10.1021/cr068000q**.
12 M. E. Porter and C. van der Linde, *J. Econ. Perspect.*, 1995, **9**, 97–118.
13 L. Harris, J. Farber, *et al.*, *Compr. Rev. Food Sci. Food Saf.*, 2003, **2**(Suppl. 1), 78–141.
14 A. K. Verma, P. R. Rout, E. Lee, P. Bhunia, J. Bae, R. Y. Surampalli, T. C. Zhang, R. D. Tyagi, P. Lin and Y. Chen, *Biodiversity and Sustainability*, Wiley, 2010.
15 F. Zahir, S. J. Rizwi, S. K. Haq and R. H. Khan, *Environ. Toxicol. Pharmacol.*, 2005, **20**, 351–360.
16 N. Zheng, Q. Wang, X. Zhang, D. Zheng, Z. Zhang and S. Zhang, *Sci. Total Environ.*, 2007, **387**, 96–104.
17 Y. Wang, F. Yang and X. Yang, *Biosens. Bioelectron.*, 2010, **25**, 1994–1998.
18 F. Di Natale, A. Lancia, A. Molino, M. Di Natale, D. Karatza and D. Musmarra, *J. Hazard. Mater.*, 2006, **132**, 220–225.
19 M. Harada, *Crit. Rev. Toxicol.*, 1995, **25**, 1–24.
20 EPA Fact Sheet EPA-823-F-01-001, *Water Quality Criterion for the Protection of Human Health: Methylmercury*, U.S. Environmental Protection Agency, Office of Water, Washington, DC, 2001, p. 1.
21 S. Bose-O'Reilly, K. M. McCarty, N. Steckling and B. Lettmeier, *Curr. Probl. Pediatr. Adolesc. Health Care*, 2010, **40**, 186–215.
22 I. M. El-Sewify, A. Radwan, N. H. Elghazawy, W. Fritzsche and H. M. Azzazy, *RSC Adv.*, 2022, **12**, 32744–32755.
23 V. Sharma, S. Dutta, R. K. Roy, S. Manna, S. M. Choudhury and G. K. Patra, *J. Mol. Struct.*, 2025, **1329**, 141398.
24 A. Pandey, D. Kumar, S. Dutta, S. Manna, S. M. Choudhury, V. Sharma and G. K. Patra, *Spectrochim. Acta, Part A*, 2025, **337**, 126104.
25 R. N. Brent, H. Wines, J. Luther, N. Irving, J. Collins and B. L. Drake, *J. Environ. Chem. Eng.*, 2017, **5**, 768–776.
26 M. Leermakers, W. Baeyens, P. Quevauviller and M. Horvat, *TrAC, Trends Anal. Chem.*, 2005, **24**, 383–393.
27 M. Sahu, V. Sharma and G. K. Patra, *Curr. Anal. Chem.*, 2024, **20**, 73–89.
28 M. Sahu, A. K. Manna and G. K. Patra, *Inorg. Chim. Acta*, 2021, **517**, 120199.
29 K. Chen, S. She, J. Zhang, A. Bayaguud and Y. Wei, *Sci. Rep.*, 2015, **5**, 16316.
30 S. Hazra, C. Bodhak, S. Chowdhury, D. Sanyal, S. Mandal, K. Chattopadhyay and A. Pramanik, *Anal. Bioanal. Chem.*, 2019, **411**, 1143–1157.

31 S. Dey, A. Kumar, S. K. Hira and P. P. Manna, *Supramol. Chem.*, 2019, **31**, 382–390.
32 M. Hong, Y. Chen, Y. Zhang and D. Xu, *Analyst*, 2019, **144**, 7351–7358.
33 Y. Wang, H. Ding, Z. Zhu, C. Fan, Y. Tu, G. Liu and S. Pu, *J. Photochem. Photobiol., A*, 2020, **390**, 112302.
34 C.-B. Bai, W.-G. Wang, J. Zhang, C. Wang, R. Qiao, B. Wei, L. Zhang, S.-S. Chen and S. Yang, *Front. Chem.*, 2020, **8**, 14.
35 J. Hu, X. Yu, X. Zhang, C. Jing, T. Liu, X. Hu, S. Lu, K. Uvdal, H.-W. Gao and Z. Hu, *Spectrochim. Acta, Part A*, 2020, **241**, 118657.
36 B. U. Gauthama, B. Narayana, B. K. Sarojini, N. K. Suresh, Y. Sangappa, A. K. Kudva, G. Satyanarayana and S. V. Raghu, *Microchem. J.*, 2021, **166**, 106233.
37 Z. Dong, X. Tian, Y. Chen, J. Hou, Y. Guo, J. Sun and J. Ma, *Dyes Pigm.*, 2013, **97**, 324–329.
38 H. Lee, H.-S. Lee, J. H. Reibenspies and R. D. Hancock, *Inorg. Chem.*, 2012, **51**, 10904–10915.
39 S. O. Aderinto, *Chem. Pap.*, 2020, **74**, 3195–3232.
40 A. Ghorai, S. S. Thakur and G. K. Patra, *RSC Adv.*, 2016, **6**, 108717–108725.
41 R. Chandra, A. Dutta, A. K. Manna, K. Rout, J. Mondal and G. K. Patra, *Inorg. Chim. Acta*, 2019, **496**, 119042.
42 V. Sharma, B. Sahu, U. K. Das and G. K. Patra, *Inorg. Chim. Acta*, 2023, **552**, 121491.
43 K. Rout, A. K. Manna, M. Sahu, J. Mondal, S. K. Singh and G. K. Patra, *RSC Adv.*, 2019, **9**, 25919–25931.
44 R. Chandra, A. K. Manna, M. Sahu, K. Rout and G. K. Patra, *Inorg. Chim. Acta*, 2020, **499**, 119192.
45 A. K. Manna, S. Chowdhury and G. K. Patra, *Dalton Trans.*, 2019, **48**, 12336–12348.
46 Y. Xiang, L. Mei, N. Li and A. Tong, *Anal. Chim. Acta*, 2007, **581**, 132–136.
47 M. Thakur, K. Ghosh, P. Choudhury, A. A. Khan, S. Mondal, N. N. Ghosh and K. Biswas, *Spectrochim. Acta, Part A*, 2023, **290**, 122271.
48 A. V. G. S. Prasad, K. Trinagaraju, B. G. Rao, Y. Usha, P. S. Reddy and P. V. Rao, *Int. J. Innovative Res. Dev.*, 2013, **2**, 38–43.
49 M. S. Bashandy, F. A. Mohamed, M. M. El-Molla, M. B. Sheier and A. H. Bedair, *Open J. Med. Chem.*, 2016, **6**, 18–35.
50 S. Mabhai, M. Dolai, S. Dey, A. Dhara, B. Das and A. Jana, *New J. Chem.*, 2018, **42**, 10191–10201.
51 B. Delley, *J. Chem. Phys.*, 2000, **113**, 7756–7764.
52 B. Delley, *J. Chem. Phys.*, 1990, **92**, 508.
53 J. P. Perdew and Y. Wang, *Phys. Rev. B: Condens. Matter Mater. Phys.*, 1992, **45**, 13244–13249.
54 D. S. Biovia, *Discovery Studio Visualizer*, San Diego, 2019.
55 A. K. Manna, S. Chowdhury and G. K. Patra, *New J. Chem.*, 2020, **44**, 10819–10832.
56 K. Rout, A. K. Manna, M. Sahu and G. K. Patra, *Inorg. Chim. Acta*, 2019, **486**, 733–741.
57 G. K. Patra and I. Goldberg, *Polyhedron*, 2002, **21**, 2195–2199.
58 A. K. Manna, J. Mondal, R. Chandra, K. Rout and G. K. Patra, *J. Photochem. Photobiol., A*, 2018, **356**, 477–488.
59 K. Ghosh, T. Sarkar and A. Samadder, *Org. Biomol. Chem.*, 2012, **10**, 3236–3243.
60 B. Sen, S. Pal, S. Lohar, M. Mukherjee, S. K. Mandal, A. R. Khuda-Bukhsh and P. Chattopadhyay, *RSC Adv.*, 2014, **4**, 21471–21478.
61 Y. Fang, Y. Zhou, J.-Y. Li, Q.-Q. Rui and C. Yao, *J. Photochem. Photobiol., A*, 2015, **215**, 350–359.
62 Y. Jiao, L. Zhang and P. A. Zhou, *Talanta*, 2016, **150**, 14–19.
63 J. Chen, Y. Li, W. Zhong, H. Wang, P. Zhang and J. Jiang, *Anal. Methods*, 2016, **8**, 1964–1967.